Heterodyne apertureless near-field scanning optical microscopy on periodic gold nanowells

Jeffrey E. Hall, Gary P. Wiederrecht and Stephen K. Gray

Chemistry Division and Center for Nanoscale Materials, Argonne National Laboratory, 9700 South Cass Avenue, Argonne, IL 60439
wiederrecht@anl.gov, gray@anl.gov

Shih-Hui Chang

Institute of Electro-Optical Science and Engineering, No. 1 University Road, Tainan City, Taiwan 701

Seokwoo Jeon,*and* John A. Rogers

Department of Materials Science and Engineering, Department of Chemistry, University of Illinois at Urbana-Champaign, Urbana, IL 61801

Renaud Bachelot and Pascal Royer

Laboratoire de Nanotechnologie et d'Instrumentation Optique, ICD CNRS FRE 2848 Université de Technologie de Troyes, 12, rue Marie Curie, BP2060.10010 Troyes cedex, France

Abstract: Heterodyne detection for apertureless near-field scanning optical microscopy was used to study periodic gold nanowell arrays. Optical near-field amplitude and phase signals were obtained simultaneously with the topography of the gold nanowells and with different polarizations. Theoretical calculations of the near-fields were consistent with the experiments; in particular, the calculated amplitudes were in especially good agreement. The heterodyne method is shown to be particularly effective for these types of periodic photonic structures and other highly scattering media, which can overwhelm the near-field scattered signal when conventional apertureless near-field scanning optical microscopy is used.

References and links

1. J. M. Brockman, B. P. Nelson and R. M. Corn, "Surface plasmon resonance imaging measurements of Ultrathin Organic Films," Annu. Rev. Phys. Chem. **51,** 41-63 (2000).
2. E. Hutter and J. Fendler, "Exploitation of Localized Surface Plasmon Resonance," Adv. Mater. **16,** 1685-1706 (2004).
3. J. Kim, J. H. Kim and K. H. Park, "Local excitation of surface plasmon in sturctured Au films by atomic force anodic oxidation," J. Vac. Sci. Technol. B **22,** 212-215 (2004).
4. S. H. Chang, S. K. Gray and G. C. Schatz, "Surface plasmon generation and light transmission by isolated nanoholes and arrays of nanoholes in thin metal films," Opt. Express **13,** 3150-1365 (2005).
5. V. Malyarchuk, F. Hua, N. H. Mack, V. T. Velesquez, J. O. White, R. G. Nuzzo and J. A. Rogers, "A High performance plasmonic crystal sensor formed by soft nanoimprint lithography," Opt. Express **13,** 5669-5675 (2005).
6. J. Homola, S. S. Yee and G. Gauglitz, "Surface plasmon resonance sensors: review," Sens. Actuators B **54,** 3-15 (1999).
7. M. E. Stewart, N. H. Mack, V. Malyarchuk, J. A. N. T. Soares, T.-W. Lee, S. K. Gray, R. G. Nuzzo and J. A. Rogers, "Quantitative multispectral biosensing and 1D imaging using quasi-3D plasmonic crystals," PNAS **103,** 17143-17148 (2006).
8. R. Quidant, G. Badenes, S. Cheylan, R. Alcubilla, J. C. Weeber, and C. Girard, "Sub-wavelength patterning of the optical near-field," Opt. Express **12,** 282-7 (2004).

9. L. Yin, V. K. Vlasko-Vlasov, A. Rydh, J. Pearson, U. Welp, S. H. Chang, S. K. Gray, G. C. Schatz, D. B. Brown and C. W. Kimball, "Surface plasmons at single nanoholes in Au films," Appl. Phys. Lett. **85,** 467-469 (2004).
10. L. Gomez, R. Bachelot, A. Bouhelier, G. P. Wiederrecht, S. H. Chang, S. K. Gray, G. Lerondel, F. Hua, S. Jeon, J. Rogers, S. Blaize, I. Stefanon and P. Royer, "Apertureless scanning Near-field Optical Microscopy: a comparison between homodyne and heterodyne approaches," J. Opt. Soc. Am. B **23,** 823-833 (2006).
11. L. Aigouy, V. Mathet, P. Beauvillainu, "Electromagnetic field distribution on a rough gold thin film: An experimental study as a function of the gold thickness," Opt. Commun. **262,** 263-269 (2006).
12. R. Bachelot, P. Gleyzes and A. C. Boccara, "Near-field optical microscope based on local perturbation of a diffraction spot," Opt. Lett. **20,** 1924-1926 (1995).
13. J. Wessel, "Surface-enhanced optical microscopy," J. Opt. Soc. Am. B **2,** 1538-1540 (1985).
14. J. Seidel, S. Grafstrom, L. Eng, L. Bischoff, "Surface plasmon transmission across narrow grooves in thin silver films," Appl. Phys. Lett. **82,** 1368-70 (2003).
15. Y. Inouye and S. Kawata, "Near-field scanning optical microscope with a metallic probe tip," Opt. Lett. **19,** 159-161 (1994).
16. F. Zenhausern, M. P. O'Boyle and H. K. Wickramasinghe, "Apertureless near-field optical microscope," App. Phys. Lett. **65,** 1623-1625 (1994).
17. R. Hillenbrand and F. Keilmann, "Near-field microscopy by elastic light scattering from a tip," Phil. Trans. R. Soc. Lond. A **362,** 787-805 (2004).
18. R. Hillenbrand and F. Keilmann, "Complex Optical Constants on a subwavelength scale," Phys. Rev. Lett. **85,** 3029-3032 (2000).
19. R. Hillenbrand and F. Keilmann, "Optical oscillation modes of plasmon particles observed in direct space by phase-contrast near-field microscopy," Appl. Phys. B **73,** 239-243 (2001).
20. G. A. Wurtz, J. S. Im, S. K. Gray and G. P. Wiederrecht, "Optical scattering from isolated metal nanoparticles and arrays," J. Phys. Chem. B **107,** 14191 (2003).
21. F. Hua, Y. Sun, A. Gaur, M. A. Meitl, L. Bilhaut, L. Rotkina, J. Wang, P. Geil, M. Shim and J. A. Rogers, "Polymer Imprint Lithography with Molecular-Scale Resolution," Nano Lett. **4,** 2467-2471 (2004).
22. A. Taflove and S. C. Hagness, *Computational Electrodynamics: The Finite-Difference Time-Domain Method* (Artech House, Boston, 2000).
23. R. Hillenbrand, F. Keilmann, P. Hanarp, D. S. Sutherland, J. Aizpurua, "Coherent imaging of nanoscale plasmon patterns with a carbon nanotube probe," Appl. Phys. Lett. **83,** 368-70 (2003).

The ability to create and detect plasmons in metal films of gold and silver has led to great interest in developing chemical and biological sensors, optical switches, and other photonic devices that use plasmons.[1-6] These abilities can be customized by adjusting the properties of the metal films through producing different sized hole-arrays, changing their periodicity, and adsorbing different organics onto the surface. Plasmon sensors could be based on monitoring the difference in the plasmon signal due to the change on the surface.[5,7] Locating the areas on the sample surface that have a high signal response would be beneficial for plasmonic sensor development. These highly sensitive areas could then be exploited to engineer better plasmonic sensors.

The highest spatial resolution method for detecting plasmons in metal films is to use near-field scanning optical microscopy (NSOM). [8-11] The use of NSOM provides the ability to get sub-diffraction limited optical resolution simultaneously with the topography, thus allowing for direct comparision. [12-20] However, near-field patterns of the types of hole arrays of relevance to the applications noted above are notoriously difficult to resolve with conventional NSOM methods because far-field scattering can overwhelm the signal. The goal of this paper is to show how the recently developed heterodyned apertureless NSOM technique resolves this difficulty [18-20], resulting in remarkably crisp amplitude images and providing phase information as well, even when a large amount of far-field scattering is present.
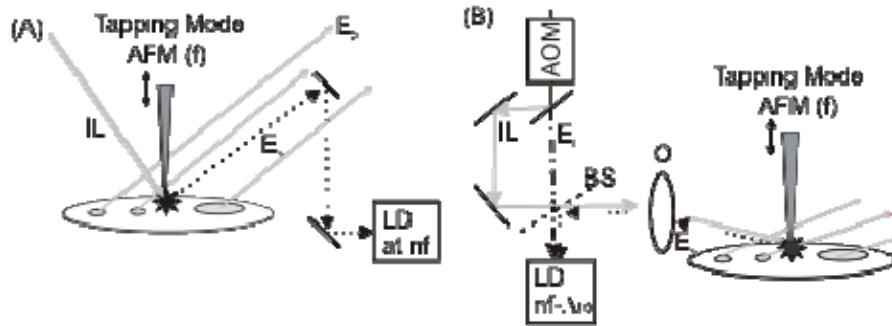
Fig. 1. (a). Schematic of homodyne detection method. IL is the incident light, E_b is the background light, E_s near-field signal from the tip-sample interaction, LD lock-in detector system. (b) Schematic of heterodyne detection method. AOM is the acousto-optical modulators, E_r is the reference beam or $\Delta\omega$, BS is a beam splitter, O is the focusing/collecting objective.

The technique used in this work is an apertureless NSOM approach using the heterodyne method for detection of the optical signal. [10, 18-20] Heterodyne detection has some highly useful advantages versus similar apertureless techniques, i.e. homodyne detection. One of these advantages is the ability to further suppress the background scattered light than the homodyne method and therefore allowing for better near-field signal contrast. Another advantage is the amplification of the near-field signal using the reference field. Both of these advantages and their derivations are fully explained in a previous paper.[10] Figure 1 diagrams the two types of apertureless NSOM. A brief description of their differences is discussed below.

Figure 1(a) shows the sample area and the detection path for the homodyne method. The incident beam from a laser source is focused at the end of an atomic force microscope (AFM) cantilever tip. This cantilever is vibrating vertically above the sample at a frequency (*f*) with amplitude of a few tens of nanometers and is positioned a few nanometers above the sample surface. Light is scattered by the extremity of the tip when encountering the sample's evanescent field. This scattered light is collected in the far-field along with any remaining incident light (dark field configuration) and detected by a photomultiplier tube (PMT). The PMT signal is fed into a lock-in detector that is set at the tapping frequency of the cantilever or one of its harmonics (*nf*) to detect the near-field signal. This signal has a complex nature as both the near-field signal and the background incident light are interrelated and cannot be easily separated, and is proportional to

$$|E_s|^2 + 2|E_s E_b|\cos(\phi_b - \phi_s),\qquad(1)$$

where E_s is the light scattered from the tip-sample interaction, E_b is the background light, ϕ_b and ϕ_s are the phase of the light from the background and tip-sample interaction, respectively. The dependence on the background signal leads to convoluted images and makes analysis of those images difficult.

Figure 1(b) illustrates the heterodyne method. [18-20] In this method the incident laser beam first passes through two acousto-optic modulators creating a second beam that is frequency shifted. The frequency shifted beam passes straight into the detection path and is designated as the reference beam ($\Delta\omega$). The incident beam is focused at the end of the AFM cantilever identical to the homodyne method. This experimental setup collects the scattered light from the tip-sample interaction back through the focusing objective and into the detection path. The signal from the sample is combined with the reference light to form a signal that is proportional to

$$2|E_s E_r|\cos(\Delta\omega t + \phi_r - \phi_s),\qquad(2)$$

where E_r is the reference light, ϕ_r and ϕ_s are the phase of the light from the reference and tip-sample interaction, respectively. The near-field amplitude and phase signals are then extracted by using a lock-in detection method at the difference of the tapping frequency and the reference beam (nf-$\Delta\omega$).

The gold nanowell sample was prepared by using an imprinting procedure. [21] Briefly, molds are formed by casting and curing a prepolymer of poly(dimethylsiloxane) (PDMS) against a "master" of photoresist on a silicon wafer, which was defined by projection mode deep ultraviolet lithography. Peeling the polymer away from the master yields a PDMS mold with the corresponding relief. In the first step of the imprinting, a layer of photocurable polyurethane is spin cast onto a glass slide. The PDMS mold is placed on top of the polyurethane. The polyurethane is then cured using ultraviolet light resulting in a solid relief structure with the same geometry of the PDMS mold. The final step in this process is to remove the PDMS mold. A thin layer of gold was blanket evaporated onto the imprinted polyurethane/glass substrate. The imprinted structure has a square lattice consisting of circular nanowells with varying diameter and periodicity. The walls of the nanowells do not have a metal coating, due to the direction flux of the electron beam evaporation system that was used.
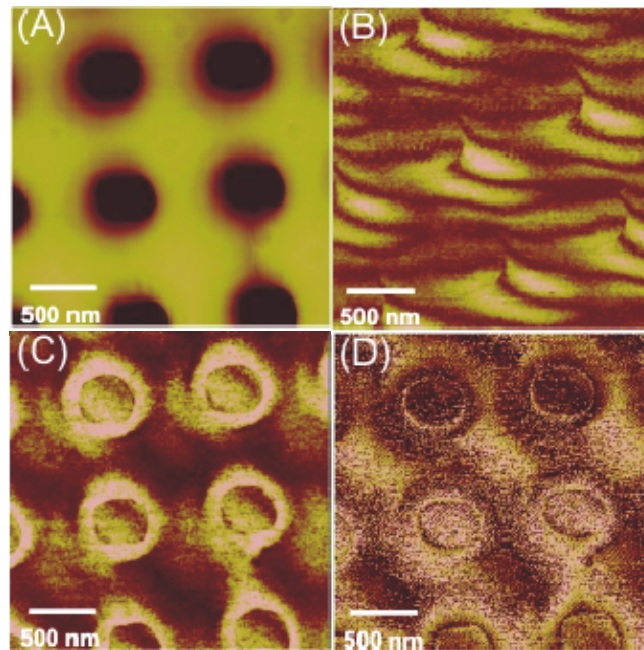

Fig. 2. NSOM images of gold nanowells. (a) Topography, (b) homodyne detected optical near-field amplitude taken at tapping mode frequency f, (c) heterodyne detected optical near-field amplitude (d) phase image taken at 2f-$\Delta\omega$.[10] The incident light travels from the bottom of the images

Figure 2 shows near-field images that were obtained on the nanowell samples using apertureless NSOM techniques. For this sample, the thickness of the Au layer is 50 nm, the nanowell depths are 400 nm, hole diameters are 450 nm, and the periodicity is 800 nm. The AFM is a Digital Instruments Multimode with a Nanoscope IIIa controller. Si cantilever tips with a conical shape were used (Nanosensors model NCH-W, resonance frequency of 330 kHz). Figure 2(a) is an AFM image of the sample. Figure 2(b) is the near-field amplitude image of the nanowells obtained at the tapping frequency (f) of the AFM cantilever. This corresponds to a homodyne detection configuration, which is dominated by fringes due to the interferometric nature of the homodyne method.[10] Figure 2(b) indicates that the nanowells

perturb the fringes, but any further analysis of the near-field information of the nanowells is difficult. Figures 2(a), 2(c), and 2(d) were all taken simultaneously using the heterodyne technique. The resulting images, obtained at the frequency difference of ($2f$-$\Delta\omega$), demonstrate the capability of the heterodyne detection method. The fringes seen in the homodyne method are completely eliminated and the resulting image is the near-field amplitude signal from the sample. [10]

Figure 2(d) is a representative image of the phase obtained for this nanowell sample. The ability to obtain phase images simultaneously with topography [Fig. 2(a)] and the near-field amplitude [Fig. 2(c)] images is advantageous due to the additional information that maybe obtained and used in correlation with the topography and amplitude images. For example, phase imaging would provide important additional information for determining the physical source of the near-field amplitude. For example, it can discern coherent origins of the optical near-field, such as plasmons, from incoherent processes such as fluorescence. The coherent process will show a phase contrast across the structure, while incoherent processes will not show a spatially varying contrast.

To better understand the experimental results, theoretical calculations were conducted by using the finite-difference time-domain (FDTD) method.[4, 22] These calculations are fully three-dimensional, include uniaxial perfectly matched layers for absorbing light scattered by the nanowell system. The total-field scattered-field method was used to launch a laser beam with a wavelength of 647.4 nm, a 6 μm spot diameter, and an incident angle of 75^0 relative to the surface normal. The large incident angle used requires a large beam diameter to produce a uniform area of intensity in the central region of the metallic film structure to be consistent with how the experiments were performed. The field information discussed is inferred from Fourier transforms of the various time-dependent field components at the frequency corresponding to the incident wavelength.

The theoretical results presented also take into account, approximately, two experimental features. First, the NSOM tip drops as it passes over a hole and therefore picks up field information from the bottom of the hole. This tip effect is accounted for as follows. Let x, y and z be Cartesian coordinates with x, y parallel to the plane of the surface and z normal to the surface. Assume the center of the nanowell is at $x = y = 0$ and let $z = z_b$ correspond to the bottom of the nanowell and $z = z_t$ be the top of the metal surface. If $F(x, y)$ is a theoretical amplitude or phase image to be compared with a corresponding experimental one, it was constructed with calculated field information for $z = z_t$ if $[x^2+y^2]^{1/2} > r_w - \Delta$, and otherwise calculated with information for $z = z_b$. Here, r_w is the radius of the nanowell and the factor Δ, which was taken to be 16 nm, accounts for the fact that the tip is cone shaped and it does not immediately drop down to the bottom of the nanowell near the outer edges. The second experimental feature that requires special attention is that the tip does not move in the x-y plane, but instead the sample is moved in the x-y plane with respect to the tip. The tip only moves in the z direction. This means that only the relative phase information between the incident wave and the scattered wave from the film is obtained. Therefore the phase calculated from the nanohole film had to be referenced to a similar calculation on an unstructured film. Other details of these calculations are similar to those of Ref. 4.

Aside from addressing the probe tip drop over the nanowell holes as outlined above, we did not take any further account of how the tip interacts with the system. Of course the presence of a tip can affect the near fields. See, however, Refs. 4 and 9 for a discussion of FDTD results on a related nanohole problem that explicitly include an aperture tip in some instances. These results showed that while some aspects of the near fields are altered by the presence of a tip, many general features of the ideal no-tip case are preserved in the full simulations. We thus consider that the tip's extremity acts as a Mie-Rayleigh particle that partially converts, by scattering, the near-field into far field without perturbing its nature. Such a perturbation could be due for example to tip-sample plasmon coupling, which is in our case very unlikely because the tip is Si while the sample is metallic. One specific area that the

probe does affect the observed images relative to the theory is that the wells appear smaller in the experimental images relative to the theoretical images. This is because the tip, due to a radius of curvature on the order of 10 nm, must entirely clear the edge of the well before dropping into the well. Thus, convolution with the tip has the effect of making the holes appear slightly smaller.

Figure 3 displays representative near-field amplitude images, both theoretical and experimental, at different incident and detected polarizations. The convention a/b is used to denote the incident polarization state, a, and detected polarization state, b. All the theoretical images are presented on the same linear thermal color scale. The level of agreement with experiment is very good. Both theory and experiment indicate that incident p polarization leads to the largest fields around the nanowell perimeters. In particular, the p/p case has the most contrast and largest rings of amplitude around the nanowells. In this case the incident polarization vector, being parallel to the plane of incidence is oscillating almost perpendicular
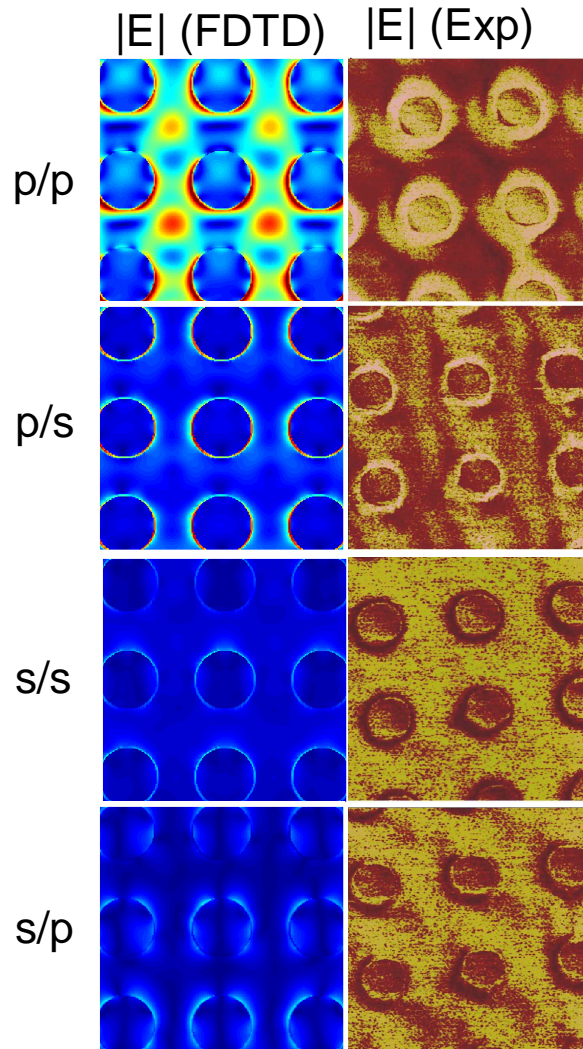

Fig. 3. Theoretical FDTD calculations and experimental NSOM images of the near-field amplitude signal of gold nanowell films. Each left-side panel is a theoretical result for the specified incident/observed polarization state, with the corresponding experimental result to its right. The incident light travels from the bottom of the images.

to the surface. It thus can excite dipolar local surface plasmon excitations along the nanowell perimeter edges that can be imagined to be oscillating up and down the nanowell sidewalls. One would expect an intense, even distribution of amplitude around the hole rims, which is observed in Fig. 3 (p/p). The theoretical p/p amplitude does show some hot spots between the nanowells that are not evident in the experimental result. These hot spots probably arise from interference of surface plasmons launched from different holes that, experimentally, are easily damped by imperfections in the holes. The p/s case also shows an even distribution around the
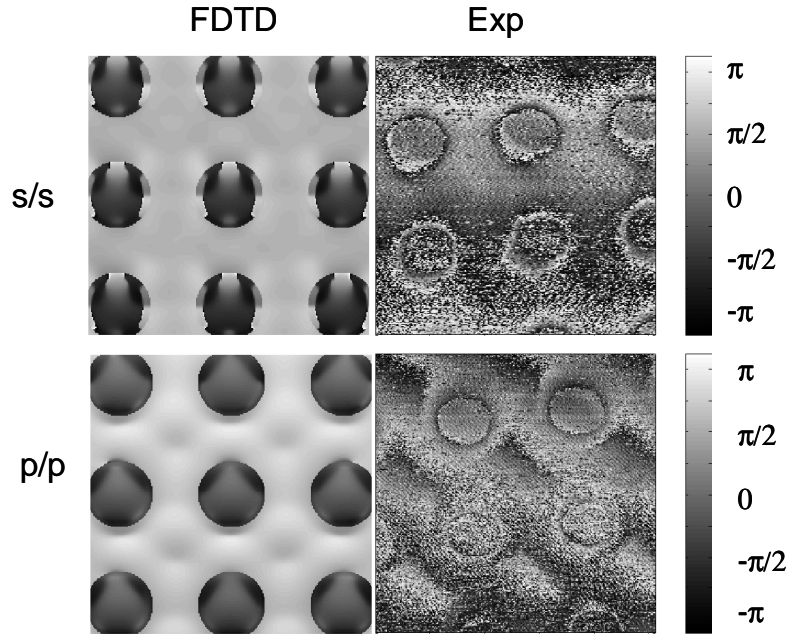

Fig. 4. Theoretical FDTD calculations and experimental NSOM images of the near-phase signal [-π, π] of gold nanowell films. Each left-side panel is a theoretical result for the specified incident/observed polarization state, with the corresponding experimental result to its right. The incident light travels from the bottom of the images

hole rims due to the p polarized illumination. Depolarization to s polarized near-field appears similar in magnitude throughout the rim. The s/s and s/p cases of Fig. 3 involve s-polarized incident light that is almost parallel to the surface and therefore do not excite such surface plasmons. It may be possible to excite dipolar local plasmon states of the holes themselves, [9] but these plasmon states are likely to be less intense, especially due to the large hole diameters studied here.

In Fig. 4, the theoretical and experimental phases for the s/s and p/p incident/detected combinations are shown. In both cases, the phase shows a change from the hole edge to the bottom of the well. Thus, the main change in phase seen is due to the difference in the optical path resulting from the tip dropping to the bottom of the nanowell. Therefore the detailed effects of any surface plasmons in the wall region are masked and one can only infer some general features. For example, in the p/p polarization case both theory and experiment indicate that the surface plasmon has the same phase all along the metal surface. While in the s/s polarization case, one would expect the local surface plasmon of the Au disk at the bottom of the well to have a π shift in phase across the hole along the polarization direction. [23] However in both our experimental and simulation data, such a phase change across the disk is not observed. However, an FDTD calculation of the absorption spectrum of the isolated disk shows that the plasmon resonance lies at approximately 500 nm. Thus, the illumination

wavelength of 647 nm is likely too far from the plasmon resonances to produce the π phase shift.

In conclusion, the heterodyne apertureless NSOM technique was used to overcome the severe difficulties encountered in measuring near fields in important nanophotonic devices such as periodic hole arrays. Remarkably crisp near-field amplitudes were found and, for the first time, simultaneous phase information was obtained for a periodic array of gold nanowells. Both the theoretical and experimental amplitude results are in good agreement and indicate that the highest near-field signal originates around the perimeter of the nanowell samples and by using p-polarization light yields the largest near-field signal. This ability to image and better understand the near fields of such systems may be applied, for example, in the continued development of plasmonic nanowell sensors.

Acknowledgments